Dual-Scale Porosity Effects on Crack Growth in Additively Manufactured Metals: 3D Ductile Fracture Models

R. Muro-Barrios, Y. Cui, J. Lambros, H.B. Chew*

Department of Aerospace Engineering, University of Illinois at Urbana-Champaign, Urbana IL 61801, USA *Author to whom correspondence should be addressed. Email: hbchew@illinois.edu

Abstract

The presence of microstructural defects resulting in unpredictable failure behavior has limited the use of additively manufactured (AM) metals in structural applications. In addition to the distributed porosity responsible for ductile fracture in conventional metals, larger defects (20-50 μm) can be introduced during additive manufacturing resulting in a dual-scale porosity failure process in AM metals. Here, we subject a three-dimensional, small-scale yielding boundary layer model containing a centerline crack to remote mode I K-field loading to study the effects of such dual-scale porosity on crack-defect interactions in an AM Ti-6Al-4V alloy. We model the background porosity implicitly within the fracture process zone viz. several rows of voidcontaining computational cell elements governed by the Gurson porous material relation, while the larger AM void defects are discretely represented based on size and porosity distributions of actual AM Ti-6Al-4V specimens characterized using optical and electron microscopy. Results show that AM defects can contribute to an increased apparent toughness of the AM metal over its conventional counterpart by activating isolated and/or clustered damage zones surrounding the crack, which shields and blunts the crack-tip and promotes crack tortuosity. However, the presence of planar clusters of AM defects can also accelerate crack growth and cause premature failure by forming preferential crack paths.

Keywords: Dual-scale voids; crack growth; void growth and coalescence; fracture toughness; additively manufactured metals; finite element method

1. Introduction

Additively manufactured (AM) metals are revolutionizing the metal-forming industry. The freeform fabrication possible through additive manufacturing allows for complex component designs often not easily achievable with traditional manufacturing methods. Despite their benefits, additive manufacturing processes can cause microstructural irregularities such as the formation of porosity (void defects), increased surface roughness, oxygen enrichment, and residual stresses that can result in variability of the mechanical, especially failure, properties of AM metals (Liu & Shin, 2019). Common additive manufacturing techniques for metallic components, for example Direct Metal Laser Melting (DMLM), are based on powder bed fusion methods. Specifically, the DMLM process deposits a layer of powder particles using a roller onto a build plate within an environment-controlled build chamber, where a laser follows a Computer Aided Design (CAD) file geometry to fully melt the powder particles and fuse them with the underlying build material (Dutta & Froes, 2016). Process parameters such as the laser scan speed, laser power, hatch spacing (the distance between subsequent laser passes), powder layer thickness, and build chamber temperature can all affect the propensity for defect formation (Casalino et al., 2015).

Void defects ~20 to 50 µm in diameter can be introduced during the DMLM process via gas entrapment, melt pool instabilities, and incomplete melting of powder particles often referred to as "lack-of-fusion" defects (Snow et al., 2020). Gas entrapment occurs when suboptimal laser parameters deposit excessive energy that vaporizes material deep below the current build layer to cause cavitation; this process often results in spherical void defects also referred to as "keyhole" defects (Panwisawas et al., 2017). In contrast, lack-of-fusion defects are typically elongated in nature and contain multiple unmelted particles (Snow et al., 2020). Proper calibration of the

additive manufacturing process parameters is especially important for complex and thin AM builds, which are susceptible to increased AM void defects due to poor heat dissipation at the build surface by the surrounding powder bed (Frydryk, 2021; Wu et al., 2020). AM components produced via DMLM are known to exhibit unpredictable mechanical failure properties due to the inclusion of such AM processing defects. In many cases, these AM metals exhibit yield strength and ultimate tensile stress rivaling those of their wrought counterparts, but with reduced ductility (Snow et al., 2020). Fatigue life also varies significantly in the individual AM specimens, even when prepared using identical AM process parameters. Of course, surface roughness plays a significant role in as-produced AM metal fatigue life, but even when polished, premature failure in AM samples is known to be caused in part by the presence of large AM void defects near the specimen surface (Foehring et al., 2018; Chastand et al., 2018; Snow et al., 2020; VanSickle et al., 2020).

In conventional metals, the nucleation, growth, and eventual coalescence of microvoids resulting in ductile fracture are well established failure processes (Faleskog & Shih, 1997). Metal alloys that fail through ductile fracture processes typically contain small inclusions or imperfections that act as nucleation sites for microvoids (2-12 µm) at low stress levels through the brittle cracking or decohesion of particulates (Stone et al., 1985). As these nucleated microvoids grow, locally intense triaxial stress fields induce the formation of new microvoids at neighboring inclusions, which in turn coalesce and form an incipient microcrack within the material. In addition to these background microvoids, the presence of additional AM defects, namely keyhole and/or lack-of-fusion defects, introduces a dual-scale porosity in the AM microstructure: the larger-scale voids (~20-50 µm in size) are the defects resulting from the additive manufacturing process while the smaller-scale voids are the intrinsic background voids

which nucleate from inclusions at low stress levels in conventional alloys. The interactions between these two scales of voids and their effect on the crack path and fracture toughness are still not well established, although their significance on AM part failure is clear (Chastand et al., 2018; Snow et al., 2020; VanSickle et al., 2020). A numerical approach that elucidates the relationships between crack-defect interactions and fracture toughness would assist in better understanding the effects of such dual-scale porosity on the failure mechanics of AM metal components.

A variety of numerical approaches have been proposed to model the micromechanical processes of void growth and coalescence that occur within the fracture process zone (FPZ) of ductile materials (Tvergaard, 1989; Faleskog et al., 1998; Tvergaard & Hutchinson, 2002; Chew et al., 2004, 2005a; Hütter et al., 2013; Zybell et al., 2014), including the implementation of single or multiple rows of voids ahead of the crack, which are modeled explicitly, or implicitly through computational cell elements. Together, these studies have provided rich insights into the ductile fracture process, such as the effects of internal porosity or internal pressure on the transition in crack growth mechanics from void-by-void to multiple-void-interaction processes (Tvergaard & Hutchinson, 2002; Chew et al., 2005b), and the effects of surrounding voids on crack-tip shielding (Hütter et al., 2013; Zybell et al., 2014). The synergistic interactions between primary and secondary inclusions during fracture of conventional metallic alloys have also been studied, using representative volume element or crack growth models containing two size-scales of voids (Chew et al., 2006; Hütter et al., 2014; Osovski et al., 2014; Srivastava et al., 2014, 2017; Tekoglu, 2015; Liu et al., 2019; Cui et al., 2020).

In this work, we explore both the 2D and 3D modeling of AM defect-crack interactions to elucidate the relationship between dual-scale porosity and fracture response of AM Ti-6Al-4V.

To accomplish this, a numerical approach in both 2D and 3D was implemented based on a small-scale yielding, modified boundary layer model with imposed monotonic K_I remote displacement loading. The intrinsic background porosity in the FPZ was modeled with multiple rows of void-containing cells governed by a modified Gurson yield criterion, while the larger AM void defects were explicitly modeled as discrete voids randomly instantiated throughout the FPZ finite element mesh at various volume fractions. Computations of the fracture resistance curves in relation to snapshots of the cross-sectional planes of void growth and material damage within the FPZ provide detailed insights into the common damage dissipation mechanisms associated with crack-defect interactions and their effects on the variability of the fracture response in AM Ti-6Al-4V.

2. Problem Formulation

2.1 Dual scale porosity in additively-manufactured Ti-6Al-4V

To illustrate the two size-scales of voids present in AM metals, we show in Fig. 1a scanning electron microscopy (SEM) image of the dimpled ductile fracture surface of an AM Ti-6Al-4V alloy fabricated by DMLM (VanSickle et al., 2020) which depicts the presence of two ~20 and ~30 µm diameter AM voids surrounded by uniformly-distributed background voids. Comparatively, only a single size-scale of voids of similar void diameters to the AM background voids are observed on the dimpled ductile fracture surface of a conventional Ti-6Al-4V in Fig. 1b. To estimate the powder particle diameters used for this AM build which we procured from GPI Prototype & Manufacturing Services, we show in Fig. 1c an SEM image of a large number of unsintered AM powder particles, and quantify the AM powder particle size distribution measured from this image in Fig. 1d.

We conduct optical microscopy imaging of cross-sections of a Ti-6Al-4V specimen material (Fig. 1e) to characterize the pre-deformation distribution of AM void diameters (Fig. 1f) and nearest neighbor distance between AM voids (Fig. 1g) over different cross-sectional cuts. Most of the AM void diameters are within a narrow 10-30 µm band. This falls within the range of metal powder particle diameters used for this AM Ti-6Al-4V build (Fig. 1d), which suggests that most of the AM voids are keyhole-type defects. However, a smaller but still discernable number of AM voids are observed to have diameters of up to 50 µm (Fig. 1f). These larger AM defects often comprise of elliptical voids or clustered groups of voids, which confirms the presence of a smaller number of lack-of-fusion-type defects in the AM Ti-6Al-4V build. To calculate an expected AM void defect volume fraction, we divide the total volume of all AM defects (assume AM void diameter of 20 µm reflecting the mean metal powder particle diameter) by the volume formed by the area of the optical micrographs times the average nearest AM void distance (assumed to be the same in all directions). The AM void defect volume fraction was estimated to be $V_f = 0.0002$, in line with expectations for a high quality, highly dense AM material manufactured using the optimal additive manufacturing process parameters (Liu & Shin, 2019; Frydryk, 2021). Because of the low AM void fraction, the material properties are still comparable to the conventional metal, though the presence of these AM voids can have a substantial effect on the crack growth response.

2.2 Boundary value problem

To investigate the role of dual porosity effects on crack growth in AM Ti-6Al-4V, we adopt a boundary layer model, with a semi-infinite centerline crack, subjected to remote mode I K-field loading under small scale yielding conditions (Fig. 2). Outside of the process zone, an

elastoplastic material response is assumed as defined by the uniaxial true stress (σ)-logarithmic strain (ϵ) relation

$$\epsilon = \frac{\sigma}{F}$$
, $\sigma < \sigma_0$

$$\epsilon = \frac{\sigma_0}{E} \left(\frac{\sigma}{\sigma_0}\right)^{\frac{1}{N}}, \sigma \ge \sigma_0 \tag{1}$$

where E is the Young's modulus, σ_0 is the yield strength, and N is the strain hardening exponent. Generalization to multiaxial stress states assumes isotropic hardening and a von Mises yield condition. In the simulations, we adopt the material parameters of E = 107 GPa, $\sigma_0 = 940$ MPa, N = 0.04, as well as a Poisson's ratio of v = 0.3 to reflect the properties of Ti-6Al-4V.

Both our 2D and 3D finite element analyses are performed using the open-source 3D finite element code WARP3D (Koppenhoefer et al., 1994). Our 2D analyses comprise of an (x_1, x_2) -plane of 8,865 8-noded brick elements of uniform thickness D along the x_3 -axis, with out-of-plane displacements $u_3 = 0$ imposed for all nodes resulting in plane strain boundary conditions. In our 3D analyses, we extrude the 2D model by 10 elements (i.e. 10D) along the x_3 -axis for a total of 88,650 elements. We conduct 3D analyses under plane strain boundary conditions by imposing roller boundary conditions on the nodes of all elements along the inner and outer plane surfaces ($x_3 = 0,10D$). Separately, we also conduct 3D analyses under plane stress boundary conditions by imposing roller boundary conditions on the nodes of all elements along the inner plane surface ($x_3 = 0$) while nodes of all elements along the outer plane surface ($x_3 = 10D$) are held traction-free. These 3D models are termed as 3D plane strain and plane stress models, respectively. Along the remote circular boundary of both the 2D and 3D finite element mesh as shown in Fig. 2c, we impose the elastic asymptotic in-plane displacement fields

$$u_1(R,\theta) = K_I \frac{1+\nu}{E} \sqrt{\frac{R}{2\pi}} \cos\left(\frac{\theta}{2}\right) \left(\kappa - 1 + 2\sin^2\left(\frac{\theta}{2}\right)\right)$$

$$u_2(R,\theta) = K_I \frac{1+\nu}{E} \sqrt{\frac{R}{2\pi}} \sin\left(\frac{\theta}{2}\right) \left(\kappa + 1 - 2\cos^2\left(\frac{\theta}{2}\right)\right)$$
 (2)

where $R^2 = x_1^2 + x_2^2$, $\theta = \tan^{-1}\left(\frac{x_2}{x_1}\right)$ for nodes on the remote boundary, and $\kappa = 3 - 4\nu$ and $\frac{3-\nu}{1+\nu}$ for the plane strain and plane stress models, respectively. The energy release rate or *J*-integral is related to the mode I stress intensity factor K_I by

$$J = K_I^2 / E^* \tag{3}$$

where $E^* = E/(1-v^2)$ and E for the plane strain and plane stress models, respectively. To verify that the small-scale yielding condition is satisfied, we compute the J-integral on several contours around the crack using the domain integral method at various loading stages (Moran and Shih, 1987), and confirm that the domain integral values were in good agreement with the value give in (3) for the prescribed value of K_I .

2.3 Fracture process zone

There are two different size-scales of voids of concern within the FPZ of AM metals: the background porosity which nucleates from inclusions and particulates responsible for the ductile fracture behavior in conventional metals, as well as the much larger AM porosity generated during additive manufacturing. To differentiate between the two size-scales of voids in AM metals, the initial background void volume fraction is referred to as f_0 , while the AM void volume fraction is referred to as V_f . We refine the finite element mesh within a rectangular grid directly ahead of the initial crack-tip representing the FPZ to capture the detailed interaction of an advancing crack with AM defects, which could result in a diffused and distributed damage region. The 2D and 3D FPZ each comprises of $120 \times 53 \times 1$ and $120 \times 53 \times 10$ ($x_1 \times x_2 \times x_3$)

elements. Each cell element constituting the background porosity has dimensions $D \times D \times D$ and implicitly contains a single spherical void of initial void volume fraction f_0 (Fig. 2b,c). These background voids are assumed to be present in the FPZ from the beginning, since they nucleate from inclusions and particles at relatively low stress levels which are well below the macroscopic stress that develops ahead of the crack front. We model these background voids implicitly, via a modified Gurson yield criterion (Gurson, 1977; Tvergaard, 1982)

$$\Phi(\sigma_e, \sigma_m, \bar{\sigma}, f) = \left(\frac{\sigma_e}{\bar{\sigma}}\right)^2 + 2q_1 f \cosh\left(\frac{3q_2\sigma_m}{2\bar{\sigma}}\right) - (1 + (q_1 f)^2) = 0 \tag{4}$$

where σ_e denotes the (Mises) equivalent stress, σ_m the mean (macroscopic) stress, $\bar{\sigma}$ the (Mises) equivalent stress of the matrix material surrounding the phenomenological void, and f is the current void volume fraction. The parameters q_1 and q_2 were found to improve the model predictions for periodic arrays of void-containing computational cells, and are taken to be 1.242 and 1.113, respectively, based on the N and σ_0/E values adopted for Ti-6Al-4V (Faleskog et al., 1998). Note that (4) reduces to the von Mises yield criterion in (1) when f = 0. The void growth rate obeys the volumetric plastic strain rate relation

$$\dot{f} = (1 - f) \operatorname{tr} \mathbf{d}^{\mathrm{p}} \tag{5}$$

where $\operatorname{tr} \mathbf{d}^p$ implies the trace of the plastic deformation rate \mathbf{d}^p . The background porosity f is governed by the void growth process described by (4) and (5). Once f reaches the critical void volume fraction $f_E = 0.2$, the WARP3D element extinction procedure is invoked to remove the cell element and to allow crack growth. Numerical studies show the results to be largely unaffected by differing values of f_E of between 0.15 and 0.25 (Xia & Shih, 1995).

Unlike nonlocal approaches where the damage zone is spread over the entire FPZ and across many elements (Seupel et al., 2020), the use of the local Gurson model inevitably confines

damage to the single row of elements ahead of the crack. Thus, the size of the void-containing computational cell D represents a material parameter, which is often interpreted as the spacing between background inclusions or voids in the metal (Xia & Shih, 1995; Gao et al., 1998). This leads to the well-known mesh dependence for finite element models using local Gurson models. Usually, this intrinsic microstructural length-scale, D, together with the background porosity, f_0 , can be regarded as phenomenological parameters chosen to give a best fit of the crack growth data from experiments. Here, we will base these parameters on metallurgical studies of the surfaces of fractured specimens (Stone et al., 1985), as mentioned below, which provides our computational cell model with a strong microstructural-basis. In our AM models, however, D has another physical interpretation. The explicit modeling of AM defects as discrete spherical voids can be numerically challenging and computationally expensive (Chew et al., 2007a, 2007b; Chew, 2014), particularly in 3D boundary layer models containing a large number of such AM voids within the process zone. Here, we model an AM void defect explicitly by deleting a single cubic computational cell directly from the pre-existing FPZ mesh (Fig. 2b,c), which is similar to the deletion of computational cells with porosity reaching $f_E = 0.2$. In this study, D is chosen to be 16 μ m, since a (16 μ m)³ cube occupies approximately the same void volume as a spherical AM void defect with a diameter near 20 µm (Fig. 1f) and because powder particles also tend to be about $\sim 20 \, \mu \text{m}$ in diameter (Fig. 1d). With this characterization of D, the initial background porosity f_0 also takes on a microstructural basis. At a background porosity of $f_0 = 0.005$, each computational cell with side length $D = 16 \mu m$, interpreted to be the spacing between voids, has an equivalent void volume fraction representing a spherical pore 3.4 µm in diameter, falling within the expected range of small-scale pore diameters (Stone et al., 1985).

In the past, void growth under physical states similar to those found in the highly stressed regions ahead of a crack have been studied through the use of representative volume elements (RVEs) (Faleskog & Shih, 1997; Chew et al., 2006). To verify the modeling simplification of using cubic rather than spherical voids in the FPZ, we perform a unit cell study comparing the stress-strain and porosity evolution for cubic versus spherical void RVEs with different initial void volume fractions, V_f . Finite element $1/8^{th}$ unit cell models (inset in Fig. 3c) were created, each containing either a spherical or cubic void, using the same elastoplastic material properties as for our boundary layer model. Finite strain deformation was used in these verification analyses, which were performed using WARP3D. The RVEs were subjected to uniaxial strain loading conditions with applied strain ϵ_{22} . The porosity and axial stress (σ_{22}) evolution were found to be nearly identical between the RVEs with spherical and cubic initial void shapes (Fig. 3), particularly at low V_f of ≤ 0.05 which is well within the range of V_f for AM void defects. These uniaxial strain boundary conditions of the RVE resemble the high triaxiality stress states of the AM voids ahead of the crack in the plane strain models, which result in the rapid cavitation and growth of AM voids. We have also performed uniaxial tension simulations of the RVE, where the lower triaxiality stress states are closer to plane stress conditions (Fig. S1 of the Supplementary Materials). Once again, we show that the porosity and stress-strain predictions are in good agreement between the cubic and spherical voids. Given the low V_f for AM void defects, a cubic void representation appears to be an acceptable substitute for modeling spherical defects in AM Ti-6Al-4V which simplifies the finite element mesh.

Small-scale yielding conditions are always maintained throughout our analyses, since the remote boundary is much larger than the computational cell element size, specifically R = 10,000D. Per ASTM standards (ASTM: E399-20a, 2000), assuming a typical fracture toughness

for wrought Ti-6Al-4V of $K_{IC} = 84$ MPa \sqrt{m} with an initial yield stress of $\sigma_0 = 940$ MPa, the required thickness to achieve plane strain conditions is estimated to be ~2.5(K_{IC}/σ_0)² = 20 mm, which is nearly 125 times the thickness of our 3D boundary layer model (10 $D = 160 \mu m$). We will examine the 3D constraint effects by separately performing 3D analyses under plane strain and plane stress boundary conditions. The latter is increasingly important for thin-walled lightweight AM structures, where the capabilities to fabricate thin walls down to 400 μm and below have been demonstrated for AM Ti-6Al-4V (Kranz et al., 2014; Wu et al., 2020), which is close to the 320 μm equivalent thickness of our 3D AM plane stress model.

3. Results

In our computations of the fracture resistance (R-) curves, we consider the projected crack length along the initial crack plane $(x_2=0)$ as the crack extension (Δa) which provides a measure of the apparent fracture toughness. In our 3D boundary layer models, crack tunneling through the process zone thickness (x_3) adds an additional complexity, and the projected crack length is based on the leading edge of the crack front. The crack is perceived to have grown when the computational cells representing the background voids in front of the propagating crack-tip reach the extinction porosity $(f_E=0.2)$. In the presence of (multiple) isolated damage zones ahead of the propagating crack, these zones are only included in the total Δa measurements when they are within two computational cells (2D) from joining the main crack.

Our modeling approach considers the presence of AM void defects as the defining feature delineating AM versus conventional Ti-6Al-4V. We first isolate the effects of background porosity by computing the *R*-curves of conventional Ti-6Al-4V, with no elements of the FPZ removed prior to the start of the simulation. Results for the 2D plane strain model in Fig. 4a (red

curves) show a brittle-type fracture response across all f_0 , where a steady-state fracture toughness (Γ_{ss}) is achieved soon after fracture initiation at $\Delta \alpha/D = 1$ (Γ_0). While decreasing f_0 marginally increases Γ_0 , its effects on Γ_{ss} are more significant at low f_0 due to increased plastic dissipation. Note the nearly two-fold increase in toughness with decrease in f_0 from 0.01 to 0.0025. In the absence of AM void defects, the deformation is homogeneous through the (x_3) thickness of the 3D fracture models of conventional Ti-6Al-4V under plane strain boundary conditions, and the resulting fracture resistance curves in Fig. 4a (blue curves) are virtually identical to those in the 2D analyses (red curves). Under plane stress boundary conditions (Fig. 4b), the fracture resistance curves have similar Γ_0 to the 2D and 3D plane strain models, but demonstrate steadily increasing $J/(\sigma_0 D)$ with Δa across all f_0 which approaches Γ_{ss} at the maximum Δa computed. The presence of smaller background porosity consistently increases $J/(\sigma_0 D)$ for the same Δa . In all cases, the cracks grow straight along $x_2 = 0$ and we obtain the expected small-scale yielding K-field stresses. The experimentally-measured fracture toughness K_{IC} of conventional Ti-6Al-4V ranges from 84 to 110 MPa \sqrt{m} (USTi, 2002; Van Hooreweder et al., 2012; Becker et al., 2015). This translates to a normalized energy release rate of $I/(\sigma_0 D)$ of 3.99 to 6.84, which lies between the predicted steady-state toughness values for our crack growth models under the assumed plane strain or plane stress boundary conditions.

3.1 Damage mechanisms under high constraint

In contrast to conventional metals, AM builds also contain additive manufacturing process defects in the form of larger voids of diameters 10-50 µm as compared to the smaller and uniformly-distributed background porosity represented in our models via computational cell elements. To better understand the effects of AM void placement on fracture toughenss in our 2D

plane strain crack growth models, representing thick AM-builds, we show in Fig. 5a the R-curves for ten random instantiations of AM void defect distributions for each of the initial AM void fractions of $V_f = 0.001$ (cross symbols) and 0.005 (circle symbols) versus that for the conventional metal ($V_f = 0$; black line). In all cases, herein, the porosity of the background voids is fixed at $f_0 = 0.005$. Each AM void instantiation was created by randomly removing a number of computational cell elements from within the FPZ based on the specified V_f . Because of the low V_f , most of the AM voids within the FPZ are surrounded completely by void-containing computational cell elements; these isolated AM voids resemble ~20 µm keyhole defects. However, the random cell element deletion can also result in rare cases of AM voids instantiating next or diagonal to each other to form void clusters resembling lack-of-fusion defects. In 17 out of 20 of these AM models (10 each for the two V_f 's chosen), the mere presence of AM voids do not significantly change the R-curves. Remarkably, however, two of these AM instantiations demonstrate a two-fold higher steady-state fracture toughness compared to the corresponding conventional material (i.e. without AM voids). Even with higher AM defect density ($V_f =$ 0.005), a number of these AM samples (e.g. #2D-2) attained higher Γ_{ss} compared to 9 of the AM samples with a five-fold lower defect density ($V_f = 0.001$).

We examine the toughening mechanisms associated with the specific AM void placements for two of the AM models (#2D-1 and #2D-2 in Fig. 5a) which attain the highest $\Gamma_{\rm ss}$ for each V_f . Figures 5b and 5c compare the porosity distributions and plastic zones (operationally defined by accumulated plastic strain $\epsilon_p \geq 0.001$) at a fixed crack extension of $\Delta a = 10D$ for #2D-1 and #2D-2 versus a reference AM material (#2D-3) which exhibits similar fracture response to conventional Ti-6Al-4V. In #2D-1 with AM void fraction $V_f = 0.001$, the presence

of an isolated AM void located diagonally above (arrow in Fig. 5b,c) the growing crack tip was found to cause a deviation in the crack path resulting in a nearly two-fold increase in local toughness from that of a conventional metal. Close examination reveals that the increase in fracture resistance occurs prior to crack path deviation, which suggests that the diagonal void first shields the growing crack-tip before coalescing, which, as seen in Fig. 5c, results in the much larger plastic wake compared to the reference AM material (#2D-3) or the conventional metal. Similar observations were made for AM #2D-2 with $V_f = 0.005$, where a clear deflection of the crack path towards a cluster of AM void defects (circle in Fig. 5b,c) resulted in a larger, and more fragmented plastic wake which appeared to be split into two distinct zones: the first at the initial crack-tip, and the second centered at a confluence of three AM void defects located at ~45° below the notch-tip (circle). Despite the increased crack path tortuosity, this clustering of AM voids resulted in a slightly smaller increase in fracture resistance compared to that induced by the single isolated AM void for #2D-1. This is potentially because of the rapid accumulation of damage (background void growth) around this cluster of AM defects and the rapid coalescence of the damage zones with the growing crack-tip. Nevertheless, these results suggest that the placement of voids near the initial crack-tip in both #2D-1 and #2D-2 resulted in significant crack path deviation and crack-tip blunting causing the larger and more diffuse plastic wakes, which account for the higher steady-state fracture toughness in both these cases. See also Movie S1 of the Supplementary Materials which depicts the evolution of von Mises stress during crack growth of #2D-1 and #2D-2 versus the response of two typical AM instantiations with the same V_f . As previously shown, a combination of tortuous crack paths and plastic dissipation tend to increase fracture toughness (Roy and Zhou, 2020). We note that not all AM void placements result in crack-tip toughening or crack tortuosity. As shown by the reference AM material #2D-3,

with an overall AM void fraction identical to #2D-2 and actually higher than #2D-1, most of the AM structure exhibited no voids near or along the crack path, resulting in similar plastic zone size and fracture response to conventional Ti-6Al-4V.

The above 2D plane strain simulations demonstrate that AM void placements can significantly change the fracture toughness. However, each AM void placement in these 2D analyses effectively represents a through-thickness AM void, and the resulting effects on the fracture resistance can be more severe than in reality. As such, we perform companion 3D simulations under plane strain boundary conditions which allow for more realistic 3D representations of AM void placements in thick AM builds. Figure 6 shows the crack growth resistance curves for 10 randomly generated distributions of AM voids within the 3D FPZ for three AM void fractions of $V_f = 0.001$, 0.005, and 0.01. As aforementioned, AM void fractions of $V_f = 0.001$ and $V_f = 0.005$ are representative of actual AM builds (Liu & Shin, 2019; Frydryk, 2021), while void fractions of $V_f = 0.01$ represent AM samples with non-optimal process parameters. Our 3D results generally show that the presence of AM voids can improve or lower the steady-state toughness, though these toughness variations are now much smaller than those from the 2D analyses. An increase in V_f generally increases the scatter in the fracture resistance, though the fracture resistance values are within ~20% of the conventional metal even for the non-optimal, high AM void porosity case of $V_f = 0.01$. Nevertheless, we observe clear AM void distributions which consistently result in higher (#3D-A1) and lower (#3D-A2) apparent fracture resistance.

To better visualize the damage caused by the advancing crack through a 3D field of AM voids, x_1 - x_3 slices are taken from the 3D models parallel to the original crack plane showing the

crack path and its effect on the material above and below. These "damage maps" show the current computational cell porosity, f, overlayed on the undeformed mesh, to provide insights into the relation between the original AM void defect location (white squares) and the final damage response. Dark red denotes elements that have porosities exceeding the extinction porosity ($f_E = 0.2$) indicating a complete loss of stress-carrying capacity. Figure 7 shows the damage maps for AM void instantiations #3D-A1 and #3D-A2 which respectively possess higher and lower fracture resistance compared to the conventional metal (Fig. 6c). While the main crack for #3D-A1 still propagates along the original $x_2 = 0$ crack plane, the presence of an AM void below (along $x_2 = -D$), as well as a cluster of AM voids above (two along $x_2 = +D$, with one above along $x_2 = +2D$), result in non-planar tortuous crack growth (Fig. 7a). These AM voids effectively shield the crack-tip and dissipate damage, which retards crack growth. Conversely for #3D-A2, the presence of multiple voids along the crack plane ($x_2 = 0$), including two AM voids instantiated next to each other to form a single, enlongated lack-of-fusion AM defect, helps facilitate crack propagation and lower the fracture resistance (Fig. 7b). Our simulations show that once the crack propagates through a region devoid of AM defects, however, the fracture resistance increases to approach the Γ_{ss} of the conventional metal. We also include the damage maps for #3D-A3 representing an AM metal with similar fracture resistance to the conventional metal (Fig. 7c). We observe that the presence of single, isolated AM voids residing on the planes $\pm D$ above and below the crack front leads to undulating cracks, though these singular AM voids appear to have limited effects on the fracture toughness. This is in contrast to the shielding contribution of AM void clusters in #3D-A1 (Fig. 7a).

3.2 Damage mechanisms under low constraint

One key advantage of AM manufacturing is the ability to fabricate thin-walled AM structures with feature sizes down to ~400 µm and below (Kranz et al., 2014; Wu et al., 2020). Here, we examine the effects of AM void placements on the damage mechanisms in our 3D models under plane stress boundary conditions, representing the low constraint effects in thinwalled AM builds. We perform crack growth simulations for 50 randomly generated distributions of AM voids within the process zone for each AM void fraction. We superpose the R-curves for all 50 samples of the same V_f in Fig. 8 (cross symbols), and show that increasing V_f generally results in higher statistical fluctuations in crack advance $(\Delta a/D)$ for the same applied K_I loading, or conversely higher fluctuations in fracture resistance at the same crack instant. We remark that some of the outliers seen in the stochastic variations in the R-curves in Fig. 8 result from crack interaction with the larger, enlongated lack-of-fusion defects, formed by the instantiation of two or more AM voids next or diagonal to one another. The R-curves averaged over all 50 3D instantiations with random distributions of AM voids (blue solid curves in Fig. 8) ultimately result in a plane stress fracture response that does not differ significantly from that of the conventional metal, i.e. with $V_f = 0$ (red dashed curve in Fig. 8). However, as in the plane strain cases studied earlier, there are specific instances where higher or lower toughness is observed due to the placement of AM voids with respect to the initial or advancing crack-tip.

AM void defects are observed to increase fracture toughness through crack-tip blunting and the promotion of crack tortuosity in the 3D plane stress models. Unlike the 3D plane strain models which attain steady-state toughness almost immediately, the low constraint effects of the plane stress models permit an increase in the fracture resistance over long crack lengths. The presence of random instantiations of AM void defects result in a jagged step increase in fracture resistance oscillating about the *R*-curve of the conventional metal. Sharp increases in the fracture

resistance $(J/\sigma_0 D)$ often correspond to a changing or blunted crack path, while rapid crack propagation with marginal increase in fracture resistance often corresponds to the rapid coalescence of the crack-tip with isolated damage zones directly ahead. Figure 9a highlights the R-curves for two 3D instantiations #3D-B1 and #3D-B2, with AM void distributions at V_f = 0.01, displaying nominally higher fracture resistance over most of the crack propagation length of $\Delta a = 50D$. For both cases, frequent oscillations of the crack path above and below the initial crack front often coincide with close groupings of AM voids and result in the persistent increased fracture resistance because of the increase in actual crack length caused by crack tortuosity. Of interest are the mechanisms underpinning the sharp spike in $I/(\sigma_0 D)$ for #3D-B1 at $\Delta a = 5D$ (nearly twice that for coventional Ti-6Al-4V) and the stepwise jumps in $J/(\sigma_0 D)$ beyond $\Delta a = 25D$, as well as the large jump in $I/(\sigma_0 D)$ near $\Delta a = 30D$ for #3D-B2. The crack for #3D-B1 initially at $x_2 = 0$ traverses upwards through 2 rows of computational cell elements to $x_2 = +2D$ almost instantaneously after initiation, only to reverse course and traverse downwards through 3 rows of computational cell elements to below the original crack plane (Fig. 9b). This tortuous crack path appears to have been triggered by the presence of 5 clustered AM voids (circle), 2 of which instantiated diagonal to one another at a distance +2D above the original crack plane (lack-of-fusion defect), with an additional 2 isolated AM voids (keyhole defects) on the plane directly below. This cluster of AM voids (circle) steers the crack to propagate on the $x_2 = +2D$ crack plane. However, the presence of an additional 3 isolated AM voids on the plane below $(x_2 = +D)$ accompanied by a cluster of 2 AM voids in close proximity on the $x_2 = -D$ plane (arrow) deviates the crack accordingly.

Similarly, #3D-B2 encounters a cluster of 4 AM voids spread across the $x_2 = +D$ and +2D planes early in the initial stages of crack propagation which causes the crack to propagate first

along the $x_2 = +D$ plane and inducing localized damage centered on the respective AM voids in the other planes (Fig. 9c). A combination of crack-tip blunting and crack tortuosity, promoted by a single AM void defect (arrow, Fig. 9c), also resulted in significant increase in fracture resistance after $\Delta a = 25D$ in #3D-B2. Accumulated damage (background void growth) surrounding this void also suggests the contribution of crack-tip shielding and the dissipation of plastic work as contributing factors to the toughness increase. The eventual tapering off of the *R*-curve to follow the average $J/(\sigma_0 D)$ versus Δa response can be associated with the crack propagating through a region free of AM void clusters. As also seen in #3D-B1, the sharp vertical jumps in toughness for #3D-B2 correspond to switching of the preferred crack planes caused by the presence of AM voids in the neighboring ($\pm 2D$) planes.

While crack growth is mostly contiguous in #3D-B1 and #3D-B2, material failure surrounding the AM void clusters in #3D-B1 also formed small isolated damage zones ahead of the crack prior to coalescing with the main crack (see circled regions in side view of the crack profiles along $x_3 = 0$ in Fig. 9d). In addition, multiple damage zones formed above and below the original crack plane help shield the crack front, dissipate energy, and improve the local fracture toughness during stable crack propagation.

On this note, many cracks also did not develop contiguously within the AM model specimens. Some of these cracks develop from multiple damage zones formed ahead of the crack-tip and on neighboring crack planes, and coalesce together with the propagating crack-tip. To illustrate this, Fig. 10a highlights the *R*-curve for #3D-B3, featuring AM void distributions at $V_f = 0.005$. An unusually steep jump in $J/(\sigma_0 D)$ is observed at $\Delta a = 10D$, contributing to an *R*-curve which largely exceeds the fracture response of the other AM samples until reaching a local steady-state toughness value near the end of the simulation. Formation of multiple damage zones

spreading across $\pm 2D$ from the current crack can be seen when comparing the damage maps for #3D-B3 across increasing crack advances: $\Delta a = 10D$, 35D, 43D and 63D (Fig. 10b). The initial toughening at $\Delta a = 10D$ is once again attributed to crack-tip blunting and deviation of the propagating crack plane caused by the presence of a single AM void located at $x_2 = +2D$, above the original crack plane (arrow). As the crack advances to $\Delta a = 35D$, a small isolated damge zone forms around a single AM void (arrow), while a cluster of 3 AM voids are observed inducing a sizable damage zone a distance of nearly 30D ahead of the current crack tip (yellow circle). Once again, 2 clustered AM voids on the $x_2 = +3D$ plane (green circle) appear to be responsible for deviating the main crack path, shifting it up from the $x_2 = +D$ plane to $x_2 = +2D$. With increasing K_I loading, a bridge of 20 computational cell elements with increasing void growth can be seen joining the large clustered damage zone to the main crack, forming a growing sheet of damage dissipating background pores. As the large clustered damage zone and main crack grow towards each other, the R-curve consistently remains higher than average. Once the main crack reaches $\Delta a = 43D$, the large clustered AM damge zone and main crack begin to rapidly coalese. Therefore, the crack appears to propagate very quickly between $\Delta a = 43D$ and $\Delta a = 63D$, manifesting itself as a plateau in the R-curve as the cracks unite.

The random instantiation of AM void defects next to one another to form AM void clusters locally increases fracture toughness by significantly curving the crack path (e.g. #3D-B1) and by dissipating considerable plastic energy through the formation of multiple unconnected damage zones ahead of the crack front (e.g. #3D-B1 and #3D-B3). At the same time, however, the presence of AM void clusters may also be responsible for reduced fracture resistance resulting in accelerated crack growth, which is also seen in our 3D plane strain models (e.g. #3D-A2). For example, instantiations #3D-B4 and #3D-B5 with AM void distributions of $V_f = 0.01$ (Fig. 11)

consistently exhibit lower fracture resistance compared to conventional Ti-6Al-4V. Damage maps for both samples show preferential crack propagation through planes with high density of AM void defects (Fig. 11b,c). Although crack tortuosity was promoted by tight clusters of AM voids on adjacent x_2 planes, any toughening resulting from this is negated by the accelerated coalescence with clusters of AM voids on the current crack plane. The formation of AM clusters may promote crack tortuosity and toughening during the initial blunting stage of crack propagation, but as the crack progresses, defect clusters can help direct the crack along the weaker fracture planes of the material. In physical AM builds, these weaker planar regions may manifest as long planar defects that often arise due to improper fusing of the powder layers, often called lack-of-fusion defects (see further discussions in Snow et al. 2020).

4. Discussion

Our simulations suggest that the primary factors governing crack growth resistance in AM Ti-6Al-4V are the locations of AM void defects and defect clusters with respect to the current crack-tip. Increasing the volume fraction of AM void defects (V_f) in Ti-6Al-4V alone does not significantly influence the overall fracture response. While the presence of randomly instantiated AM voids can momentarily increase or decrease the local toughness, fracture resistance gradually tapers towards the conventional Ti-6Al-4V response once the crack propagates past the AM void defects and defect clusters into a region relatively free of AM defects. This is especially apparent for AM materials with low void fractions, such as $V_f = 0.001$, under both high (plane strain) and low (plane stress) constraint conditions. However, certain AM void defect distributions can induce prolonged periods of significantly higher or lower local material toughness during crack propagation, suggesting the possibility of controlling the AM materials toughness response by strategic placement of AM defects throughout the material. In particular,

our simulations show that the presence of AM void defects located up to 2D (i.e. 2 AM void diameters) above or below the current crack plane ahead of a propagating crack tip may (a) blunt the crack tip without actually joining the crack, (b) coalesce with the crack and induce crack path tortuosity, or (c) dissipate energy through formation of isolated or clustered damage zones. Collectively, these mechanisms contribute to an increase in apparent fracture toughness. At the same time, planar AM void clusters that more closely resemble the elongated voids stemming from lack-of-fusion in the AM build are also capable of creating planes of preferential cracking and allowing a crack to rapidly propagate through the material. This phenomenon is observed under both plane stress (Fig. 11) or plane strain (Fig. 7b) boundary conditions, and thus is relevant to both thick and thin AM builds. Delineating the specific AM void placements that lead to unstable crack propagation, or significant toughening, can provide critical insights to the physical processes responsible for the variation and unpredictability in material fracture toughness in AM parts.

We show in Fig. 12a two of many possible approaches for increasing the local fracture toughness in a 2D plane strain AM model: (1) sinusoidal AM void defect placement, as first studied in Srivastava et al. (2017), promotes a winding crack path that is longer and can potentially increase the amount of plastic energy dissipated, and (2) AM void alignment following the contours of highest equivalent stress, which attempts to distribute and dissipate damage more uniformly throughout the process zone and also extend the overall size of plastically deforming material. Through the creation of stress concentrations at each AM void defect and between void clusters, there is evidence of significantly increased fracture toughness and energy dissipation over conventional metals in such strategic AM material designs (Fig. 12b). Both these design strategies seem to suggest that vertically orientated AM void clusters

tend to cause crack-tip blunting, which can be attributed to void-shielding effects, where the stress magnitude at the crack-tip is reduced by increased plastic deformations in the void array (Hütter et al., 2013, 2015; Zybell et al., 2014). This is in contrast to horizontally orientated AM void clusters which tend to create preferential planes for rapid crack growth (Figs. 7b and 11).

The 2D AM models provide clear insights into the interactions between the growing crack and AM void defect placements. Under the imposed plane strain boundary conditions, these 2D models are representative of the crack growth mechanics occurring in thick 3D AM builds. However, the obtained fracture resistance curves from these 2D models are more qualitative than quantitative. This is because the AM porosities in the 2D analyses represent the average throughthickness porosities in a real sample, but the AM voids are sparsely distributed in an actual AM specimen with finite thickness. As demonstrated by our 3D models under plane strain boundary conditions, potential toughening effects associated with AM void placements are significantly overestimated by the 2D models. Moreover, the actual stress state is three dimensional, and the nonlinear fracture process will be determined by the response of the material near a macroscopic crack tip to different stress components (e.g. Mises effective stress, hydrostatic stress, and the maximum principal stress). In particular, the primary damage mechanism of void growth and coalescence in AM metals, as evidenced by the dimpled fracture surfaces of AM Ti-6Al-4V in Fig. 1a (VanSickle et al., 2020), is governed by the hydrostatic stress component. This results in a strong three dimensionality effect on the nonlinear fracture process zone in a finite-thickness specimen, as shown in our 3D AM models under plane stress boundary conditions, representing thin-walled AM builds. The higher hydrostatic stress state due to the higher constraint in the mid-plane ($x_3 = 0$) of the 3D plane stress AM model tends to promote more intense void growth and damage relative to that at the free surface of the model ($x_3 = 10D$). Thus, the crack front on

the crack plane is usually curved, although the presence of AM voids forming localized damage clusters closer to the free surface of the model can reduce the extent of this curvature. Therefore, the effects of three dimensionality should also be considered in the formulation of design strategies through void placements to control the crack path and ultimately the fracture resistance of the material.

5. Conclusions

In this work, the relationships between dual-scale porosity and crack-defect interactions in AM Ti-6Al-4V were examined through 2D and 3D numerical simulations that were able to capture the void growth, interaction, and coalescence mechanisms in both thin- and thick-walled AM builds. These intricate mechanisms ultimately resulted in crack path tortuosity, as well as variation in fracture resistance – both phenomena that have been observed in actual AM Ti-6Al-4V specimens (VanSickle et al., 2020). Varying the levels of AM defects within a range typically seen in modern additive manufacturing processes did not significantly influence the *average* fracture response of AM instantiations in either the 2D or 3D case. However, the *variability* in fracture response increased with increasing levels of AM void defects in both the 2D and 3D models, particularly for larger void fractions when the probability of forming AM void clusters increases. These AM void clusters resemble the elongated and larger lack-of-fusion defects, while the smaller isolated AM voids represent keyhole defects from gas entrapment.

Damage mechanisms resulting from crack-defect interactions between AM void defects and background microvoids, along with their impact on the fracture resistance of AM models, were identified. AM void defects flanking a propagating crack (up to 2 AM void diameters above or below the crack plane) can blunt the crack tip and dissipate plastic energy through significant void growth around AM voids without joining with the crack. AM voids clustered ahead of the

crack can also create large, isolated damage zones that grow through microvoid coalescence and result in prolonged periods of crack growth where the local fracture toughness exceeds that of conventional alloys until rapid coalescence with the main crack occurs. Perhaps the most impactful crack-defect toughening mechanism identified during crack propagation is crack path deviation. Clusters of AM void defects located above or below the main crack plane tend to coalesce with the advancing crack tip to cause significant deviations from the original crack plane. Because the tortuous crack path is significantly longer than a planar crack path, the process results in a greater dissipation of plastic work. However, crack tortuosity can also facilitate fracture depending on the location and concentration of AM voids. Vertically orientated AM void clusters tend to cause crack-tip blunting, while horizontally orientated AM void clusters create preferential planes for rapid crack growth. Premature failure of AM Ti-6Al-4V fatigue specimens seen in experiments (e.g. VanSickle et al., 2020) may be the result of curving crack paths that are "drawn" to these weaker locations in the material. Through harnessing these crack-defect interactions of the dual-scale porosity found in AM alloys, material design using strategic void placement suggests that future AM components may purposefully include void defects to produce superior fracture resistance over conventional alloys.

Acknowledgements

The authors acknowledge the support provided by National Science Foundation under grant nos. NSF-CMMI-2009684 (HBC, RMB, YC) as well as NSF-CMMI-2027082 (JL).

References

ASTM: E399-20a (2000). Standard method of test for plane-strain fracture toughness of metallic materials. Book of Standards, Vol. 03.01.

Becker, T. H., Beck, M., & Scheffer, C. (2015). Microstructure and mechanical properties of direct metal laser sintered Ti-6Al-4V. *The South African Journal of Industrial Engineering*, 26(1), 1.

- Casalino, G., Campanelli, S. L., Contuzzi, N., & Ludovico, A. D. (2015). Experimental investigation and statistical optimisation of the selective laser melting process of a maraging steel. *Optics & Laser Technology*, 65, 151–158.
- Chastand, V., Quaegebeur, P., Maia, W., & Charkaluk, E. (2018). Comparative study of fatigue properties of Ti-6Al-4V specimens built by electron beam melting (EBM) and selective laser melting (SLM). *Materials Characterization*, 143, 76–81.
- Chew, H. B. (2006). Effects of pressure-sensitivity and plastic dilatancy on void growth and interaction. *International Journal of Solids and Structures*, 43 (21), 6380-6397.
- Chew, H. B. (2014). Cohesive zone laws for fatigue crack growth: Numerical field projection of the micromechanical damage process in an elasto-plastic medium. *International Journal of Solids and Structures*, 51 (6), 1410-1420.
- Chew, H. B., Guo, T.F., & Cheng, L. (2004). Vapor pressure and residual stress effects on toughness of polymeric adhesive joints. *Engineering Fracture Mechanics*, 71 (16-17), 2435-2448.
- Chew, H. B., Guo, T. F., & Cheng, L. (2005a). Vapor pressure and residual stress effects on mixed mode toughness of an adhesive film. *International Journal of Fracture*, 134 (3), 349-368.
- Chew, H. B., Guo, T. F., & Cheng, L. (2005b). Vapor pressure and residual stress effects on failure of an adhesive film. *International Journal of Solids and Structures*, 42(16–17), 4795–4810.
- Chew, H. B., Guo, T. F., & Cheng, L. (2007a). Pressure-sensitive ductile layers –I. Modeling the growth of extensive damage. *International Journal of Solids and Structures*, 44(7-8), 2553-2570.
- Chew, H. B., Guo, T. F., & Cheng, L. (2007b). Pressure-sensitive ductile layers –II. 3D models of extensive damage. *International Journal of Solids and Structures*, 44(16), 5349-5368.
- Cui, Y., Gao, Y. F., & Chew, H. B. (2020). Two-scale porosity effects on cohesive crack growth in a ductile media. *International Journal of Solids and Structures*, 200–201, 188–197.
- Dutta, B., & Froes, F. H. (2016). *Additive manufacturing of titanium alloys: State of the art, challenges and opportunities*. ISBN: 978-0-12-804782-8.
- Faleskog, J., Gao, X., & Shih, C. F. (1998). Cell model for nonlinear fracture analysis I. Micromechanics calibration. *International Journal of Fracture*, 89(4), 355–373.
- Faleskog, J., & Shih, C. F. (1997). Micromechanics of coalescence—I. Synergistic effects of elasticity, plastic yielding and multi-size-scale voids. *Journal of the Mechanics and Physics of Solids*, 45(1), 21–50.
- Foehring, D., Chew, H. B., & Lambros, J. (2018). Characterizing the tensile behavior of additively manufactured Ti-6Al-4V using multiscale digital image correlation. *Materials Science and Engineering: A*, 724, 536–546.
- Frydryk, D. (2021). Get the Facts on... Porosity in Metal Additive Manufacturing | GE Additive. (2021, March 10). https://www.ge.com/additive/blog/get-facts-porosity-metal-additive-manufacturing
- Gao, X., Faleskog, J., & Shih, C. F. (1998). Cell model for nonlinear fracture analysis II. Fracture- process calibration and verification. *International Journal of Fracture*, 89(4), 375–398.
- Gurson, A. L. (1977). Continuum Theory of Ductile Rupture by Void Nucleation and Growth: Part I—Yield Criteria and Flow Rules for Porous Ductile Media. *Journal of Engineering Materials and Technology*, 99(1), 2–15.

- Hütter, G., Zybell, L., & Kuna, M. (2015). Micromechanisms of fracture in nodular cast iron: From experimental findings towards modeling strategies A Review. *Engineering Fracture Mechanics*, 144, 118-141.
- Hütter, G., Zybell, L., & Kuna, M. (2014). Size effects due to secondary voids during ductile crack propagation *International Journal of Solids and Structures*, 51, 839-847.
- Hütter, G., Zybell, L., Mühlich, U., & Kuna, M. (2013). Consistent simulation of ductile crack propagation with discrete 3D voids. *Computational Materials Science*, 80, 61-70.
- Koppenhoefer, K. C., Gullerud, A. S., Ruggieri, C., Dodds, R. H., & Healey, B. E. (1994). WARP3D: Dynamic Nonlinear Analysis of Solids Using a Preconditioned Conjugate Gradient Software Architecture. https://www.ideals.illinois.edu/handle/2142/14220
- Kranz, J., Kranz, J., Herzog, D., & Emmelmann, C. (2015). Design guidelines for laser additive manufacturing of lightweight structures in TiAl6V4. *Journal of Laser Applications*, 27, S14001.
- Liu, S., & Shin, Y. C. (2019). Additive manufacturing of Ti6Al4V alloy: A review. *Materials & Design*, 164, 107552.
- Liu, Y., Zheng, X., Osovski, S., & Srivastava, A. (2019). On the micromechanism of inclusion driven ductile fracture and its implications on fracture toughness. *Journal of the Mechanics and Physics of Solids*, 130, 21-34.
- Moran, B., & Shih, C. F. (1987). A general treatment of crack tip contour integrals. *International Journal of Fracture*, 35, 363-371.
- Osovski, S., Srivastava, A., Ponson, L., Bouchaud, E., Tvergaard, V., Ravi-Chandar, K., & Needleman, A. (2015). The effect of loading rate on ductile fracture toughness and fracture surface roughness. *Journal of the Mechanics and Physics of Solids*, 76, 20-46.
- Panwisawas, C., Perumal, B., Ward, R. M., Turner, N., Turner, R. P., Brooks, J. W., & Basoalto, H. C. (2017). Keyhole formation and thermal fluid flow-induced porosity during laser fusion welding in titanium alloys: Experimental and modelling. *Acta Materialia*, 126, 251–263.
- Roy, U., & Zhou, M. (2020). A computational framework for predicting the fracture toughness of metals as function of microstructure. *Journal of the Mechanics and Physics of Solids*, 142, 103955.
- Seupel, A., Hütter, G., & Kuna, M. (2020). On the identification and uniqueness of constitutive parameters for a non-local GTN-model. *Engineering Fracture Mechanics*, 229, 106817.
- Snow, Z., Nassar, A. R., & Reutzel, E. W. (2020). Invited Review Article: Review of the formation and impact of flaws in powder bed fusion additive manufacturing. *Additive Manufacturing*, 36, 101457.
- Srivastava, A., Osovski, S., & Needleman, A. (2017). Engineering the crack path by controlling the microstructure. *Journal of the Mechanics and Physics of Solids*, 100, 1–20.
- Srivastava, A., Ponson, L., Osovski, S., Bouchaud, E., Tvergaard, V., & Needleman, A. (2014). Effect of inclusion density on ductile fracture toughness and roughness. *Journal of the Mechanics and Physics of Solids*, 63, 62–79.
- Stone, R. H. V., Cox, T. B., Low, J. R., & Psioda, J. A. (1985). Microstructural aspects of fracture by dimpled rupture. *International Metals Reviews*, 30(1), 157–180.
- Tekoglu, C. (2015). Void coalescence in ductile solids containing two populations of voids. *Engineering Fracture Mechanics*, 147, 418-430.
- Tvergaard, V. (1989). Material Failure by Void Growth to Coalescence. In J. W. Hutchinson & T. Y. Wu (Eds.), *Advances in Applied Mechanics* (Vol. 27, pp. 83–151). Elsevier.

- Tvergaard, V. (1982). On localization in ductile materials containing spherical voids. *International Journal of Fracture*, 18(4), 237–252.
- Tvergaard, V. (2002). Two mechanisms of ductile fracture: Void by void growth versus multiple void interaction. *International Journal of Solids and Structures*, 39(13), 3581-3597.
- USTi (2002). Titanium Alloys—Ti6Al4V Grade 5. *U.S. Titanium Industry Inc.* https://www.azom.com/properties.aspx?ArticleID=1547
- Van Hooreweder, B., Moens, D., Boonen, R., Kruth, J.-P., & Sas, P. (2012). Analysis of Fracture Toughness and Crack Propagation of Ti6Al4V Produced by Selective Laser Melting. *Advanced Engineering Materials*, 14(1–2), 92–97.
- VanSickle, R., Foehring, D., Chew, H. B., & Lambros, J. (2020). Microstructure effects on fatigue crack growth in additively manufactured Ti–6Al–4V. *Materials Science and Engineering:* A, 795, 139993.
- Wu, Z., Narra, S. P., & Rollett, A. (2020). Exploring the fabrication limits of thin-wall structures in a laser powder bed fusion process. *The International Journal of Advanced Manufacturing Technology*, 110(1), 191–207.
- Xia, L, & Shih, C. F. (1995). Ductile crack growth-I. A numerical study using computational cells with microstructurally-based length scales. *Journal of the Mechanics and Physics of Solids*, 43(2), 233–259.
- Zybell, L., Hütter, G., Linse, T., Mühlich, U., & Kuna, M. (2014). Size effects in ductile failure of porous materials containing two populations of voids. *European Journal of Mechanics /A Solids*, 45, 8–19.

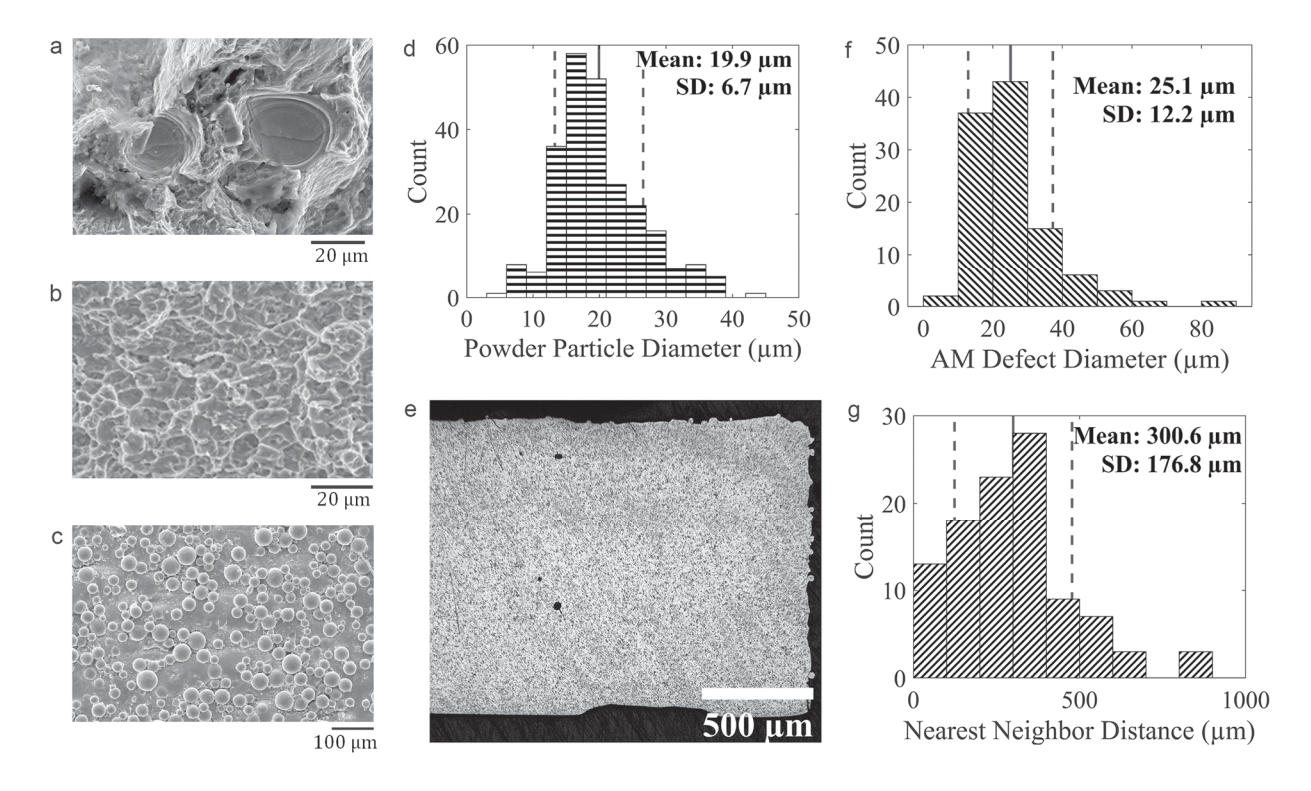


FIG. 1: (a) SEM imaging of the fracture surface of AM Ti-6Al-4V depicting two large AM voids surrounded by background voids. (b) SEM imaging of the fracture surface of conventional Ti-6Al-4V with only background voids. (c) SEM imaging of unsintered powder particles on an unfinished, as-built AM Ti-6Al-4V surface. (d) Distributions of AM powder particle diameters for Ti-6Al-4V based on (c). (e) Cross-section of an AM Ti-6Al-4V specimen by optical microscopy. (f,g) Distributions of AM void defect diameters and nearest neighbor distances between AM voids from optical microscopy. Solid lines in (d,f,g) are the mean values; dashed lines are the standard deviations (SDs).

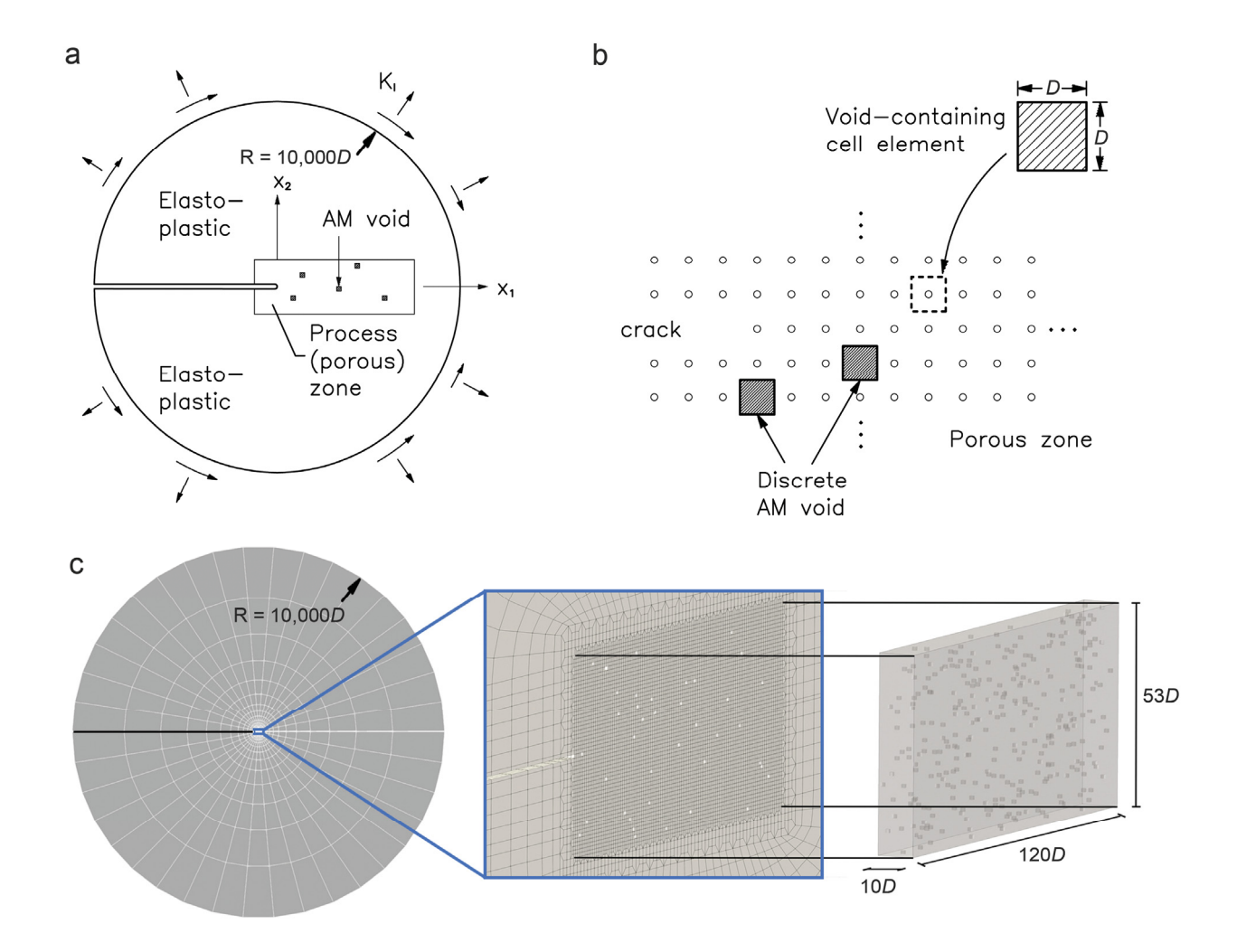


FIG. 2: (a) Boundary layer model with a centerline crack subjected to remote mode I ($K_{\rm I}$) loading. (b) Close-up view of the dual-porosity fracture process zone comprising of multiple rows of void-containing computational cell elements governed by the Gurson model, which constitute the background voids, as well as randomly distributed discrete AM voids. (c) Finite element mesh with close up view of the process zone for the 3D AM model, highlighting the 3D distributions of AM voids.

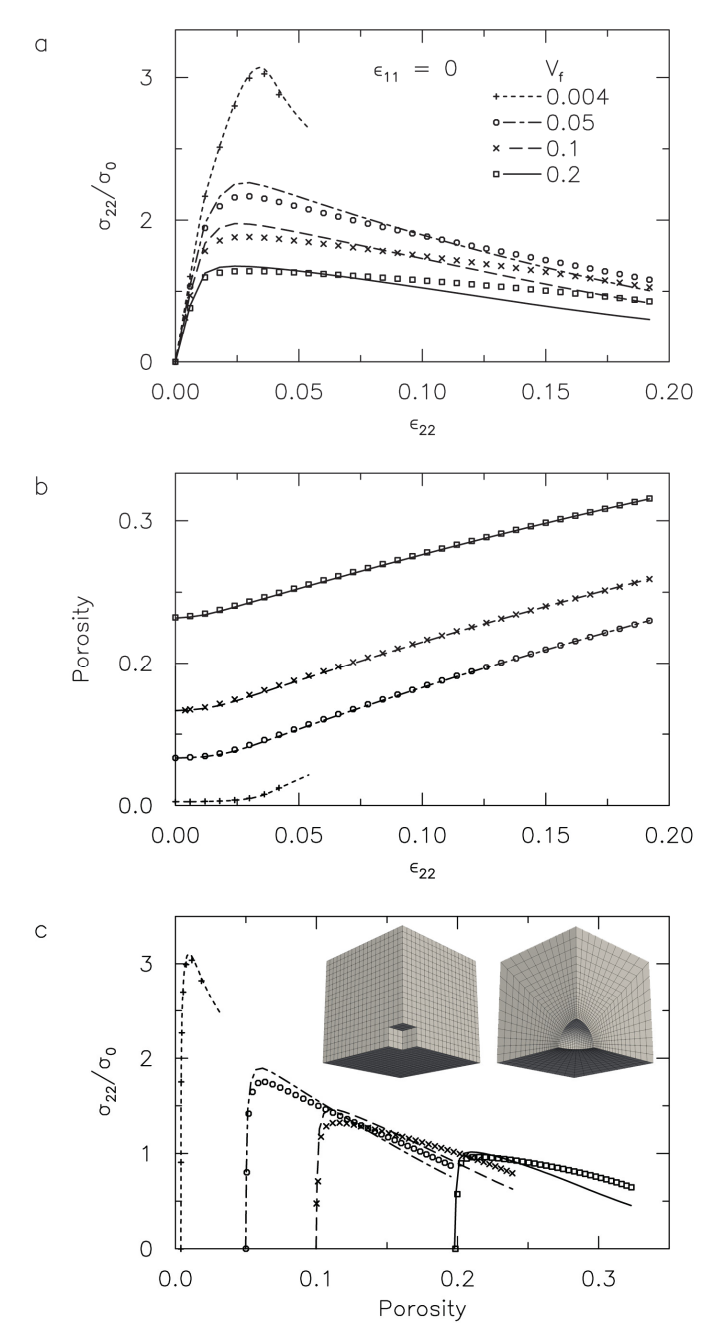


FIG. 3: Comparison of axial stress versus strain (a), porosity versus strain (b), and axial stress versus porosity (c) response, between representative volume elements (RVEs) containing cubic (lines) or spherical (symbols) voids of volume fraction V_f subjected to uniaxial straining. Inset in (c) denotes the finite element mesh of the RVEs.

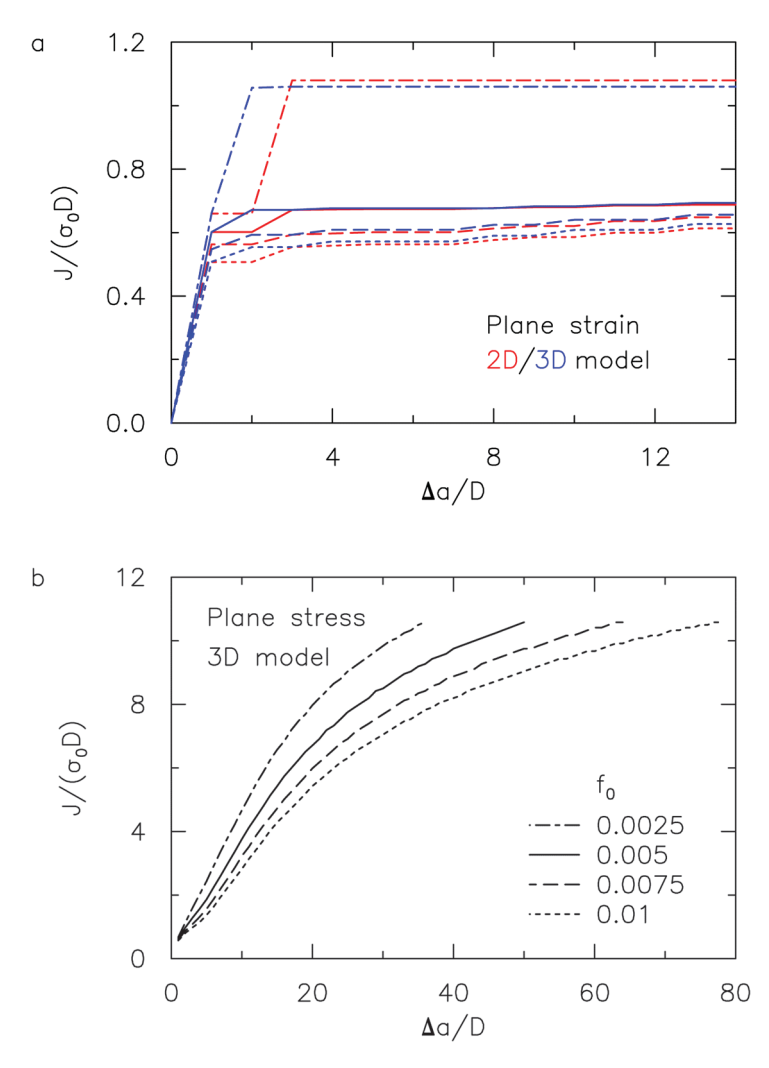


FIG. 4: Crack growth resistance curves for 2D and 3D plane strain (a) and 3D plane stress (b) models of conventional Ti-6Al-4V with different background porosities f_0 .

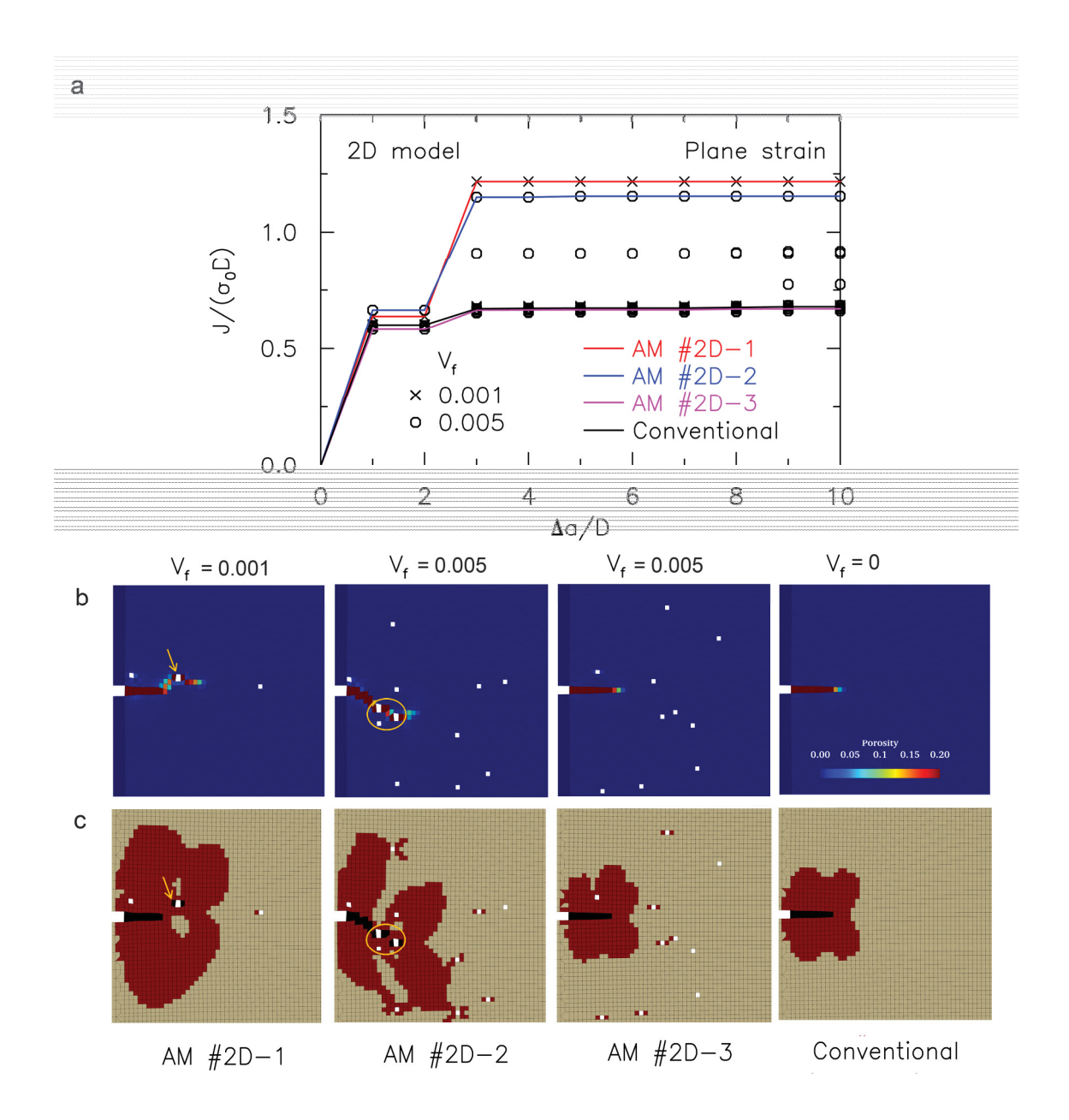


FIG. 5: (a) Crack growth resistance curves for 2D plane strain models of AM Ti-6Al-4V containing ten random instantiations of AM void defect distributions for two initial AM void fractions V_f . The background porosity is fixed at $f_0 = 0.005$ in all cases. (b,c) Porosity and accumulated plastic zone size at $\Delta a = 10D$ for three AM models (#2D-1, #2D-2, #2D-3) and the conventional Ti-6Al-4V. White squares in (b,c) denote the AM voids.

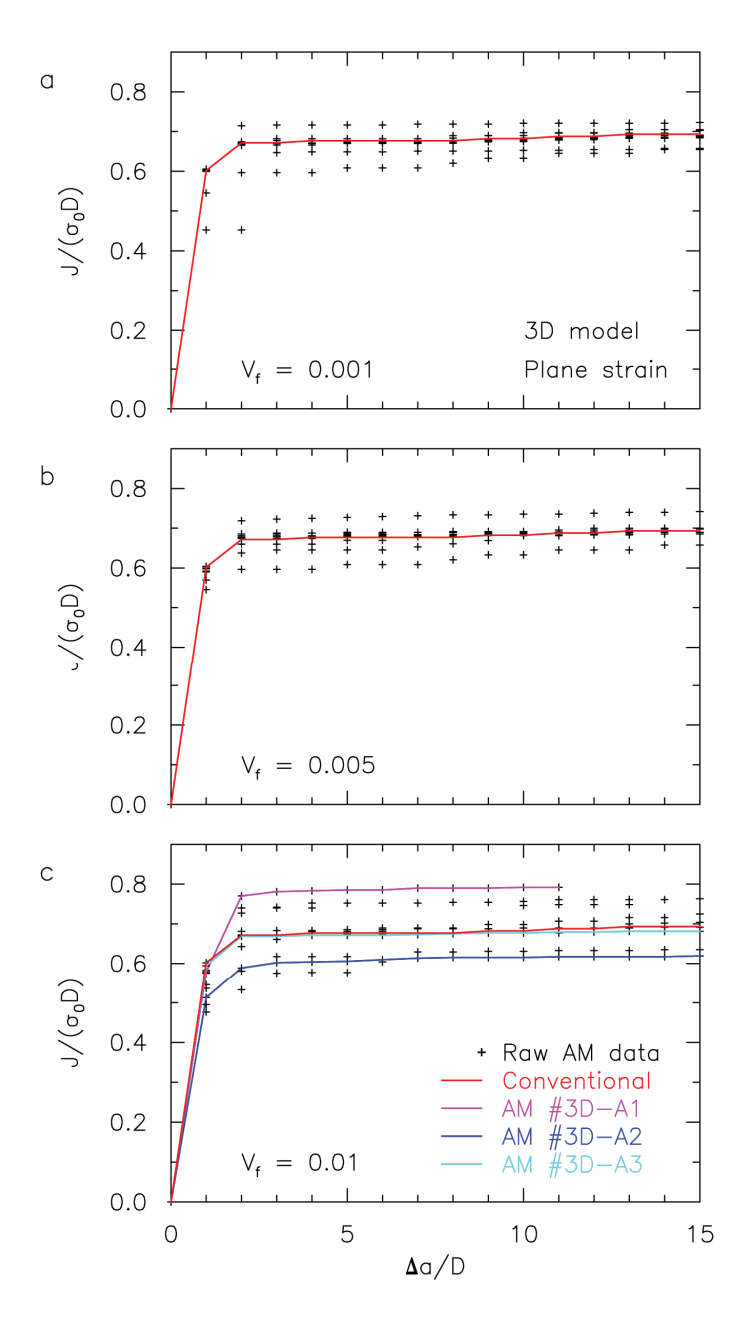


FIG. 6: Crack growth resistance curves for 3D plane strain models of AM Ti-6Al-4V of different AM void fraction V_f , each containing 10 random instantiations of AM void defect distributions (symbols). Conventional Ti-6Al-4V response denoted by red lines. The background porosity is fixed at $f_0 = 0.005$ in all cases.

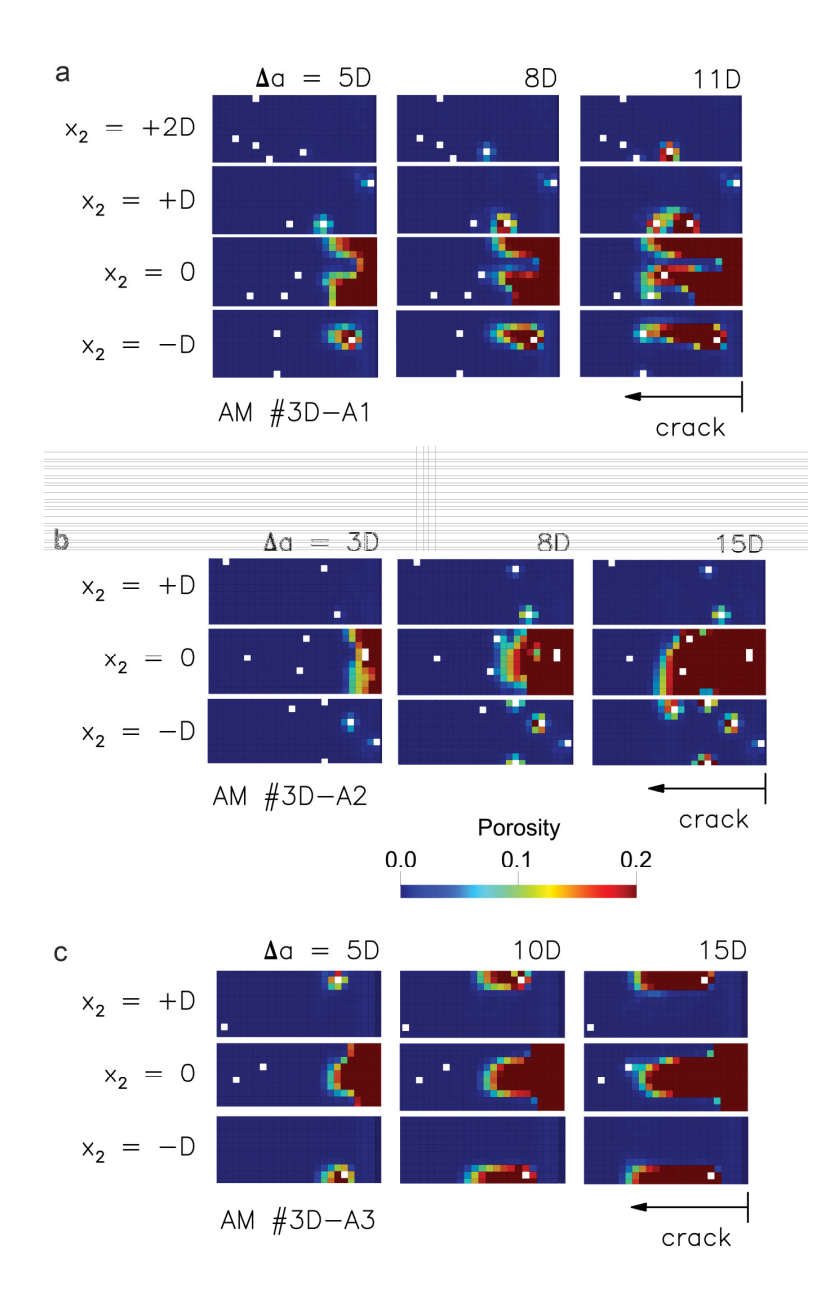


FIG. 7: Progression of damage associated with crack-defect interactions at various Δa for plane strain AM models #3D-A1, #3D-A2, and #3D-A3 with $V_f = 0.01$. White squares denote the AM voids.

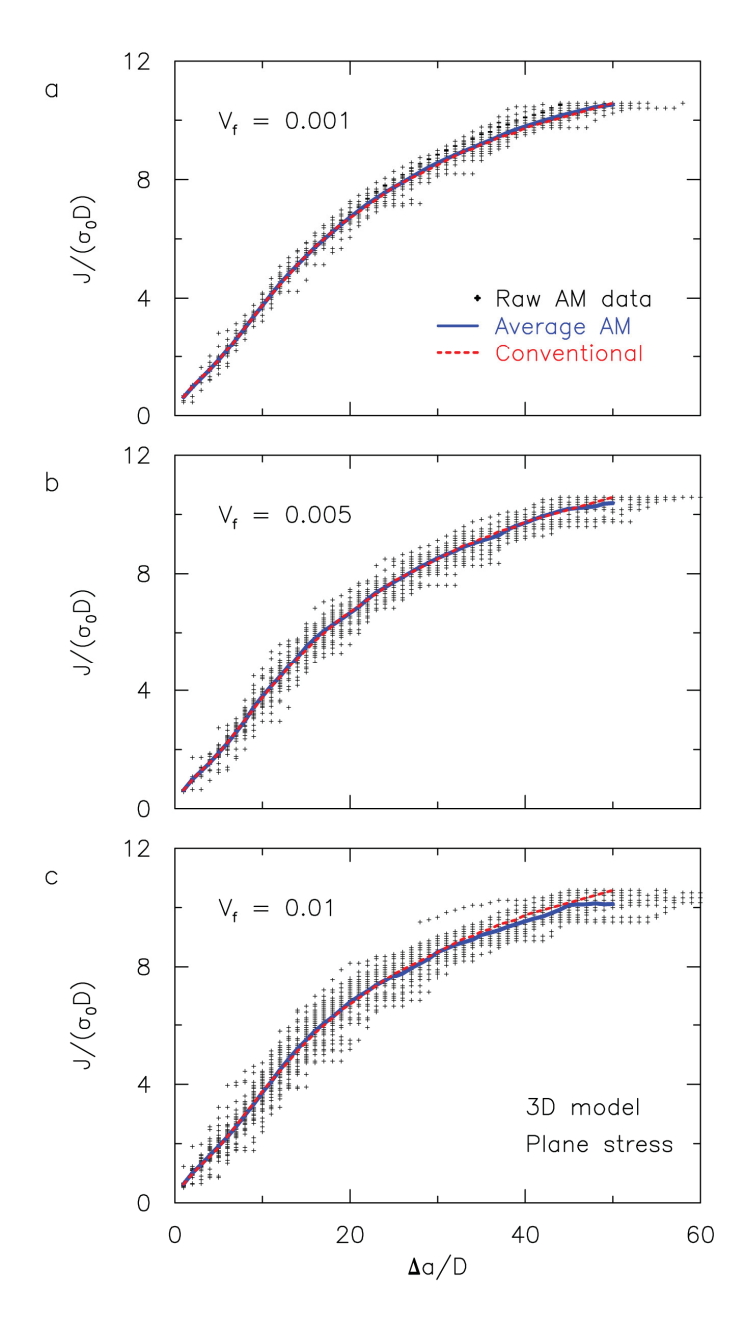


FIG. 8: Crack growth resistance curves for 3D plane stress models of AM Ti-6Al-4V of different AM void fraction V_f , each containing 50 random instantiations of AM void defect distributions (symbols), with blue lines representing the averaged response. Conventional Ti-6Al-4V response denoted by red dashed lines. The background porosity is fixed at $f_0 = 0.005$ in all cases.

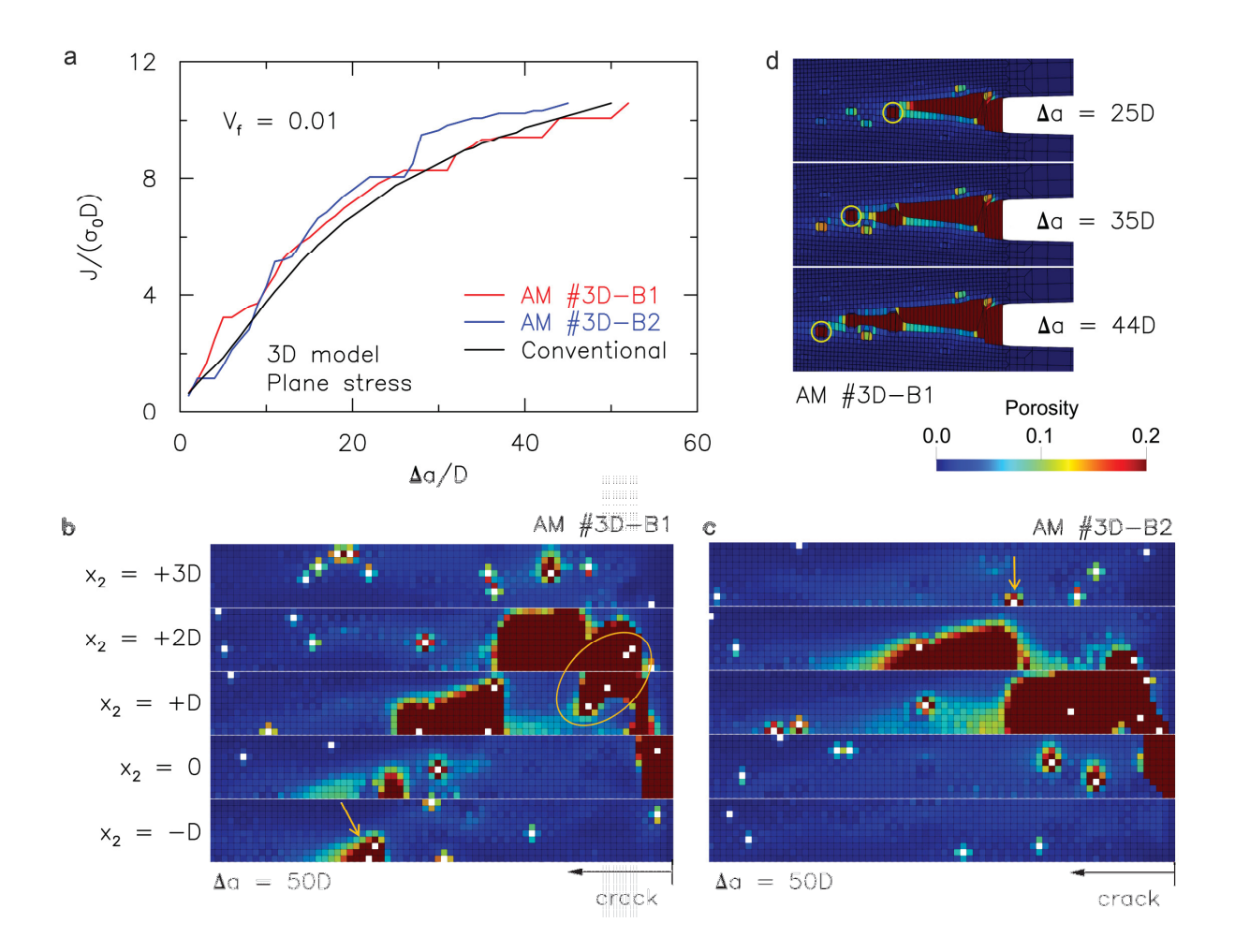


FIG. 9: Crack-defect interaction for plane stress AM models #3D-B1 and #3D-B2 with $V_f = 0.01$. (a) Fracture resistance curves. (b,c) Damage maps for #3D-B1 and #3D-B2 at $\Delta a = 50D$. White squares denote the AM voids. (d) Cross-sectional views along $x_3 = 0$ at various Δa for AM #3D-B1.

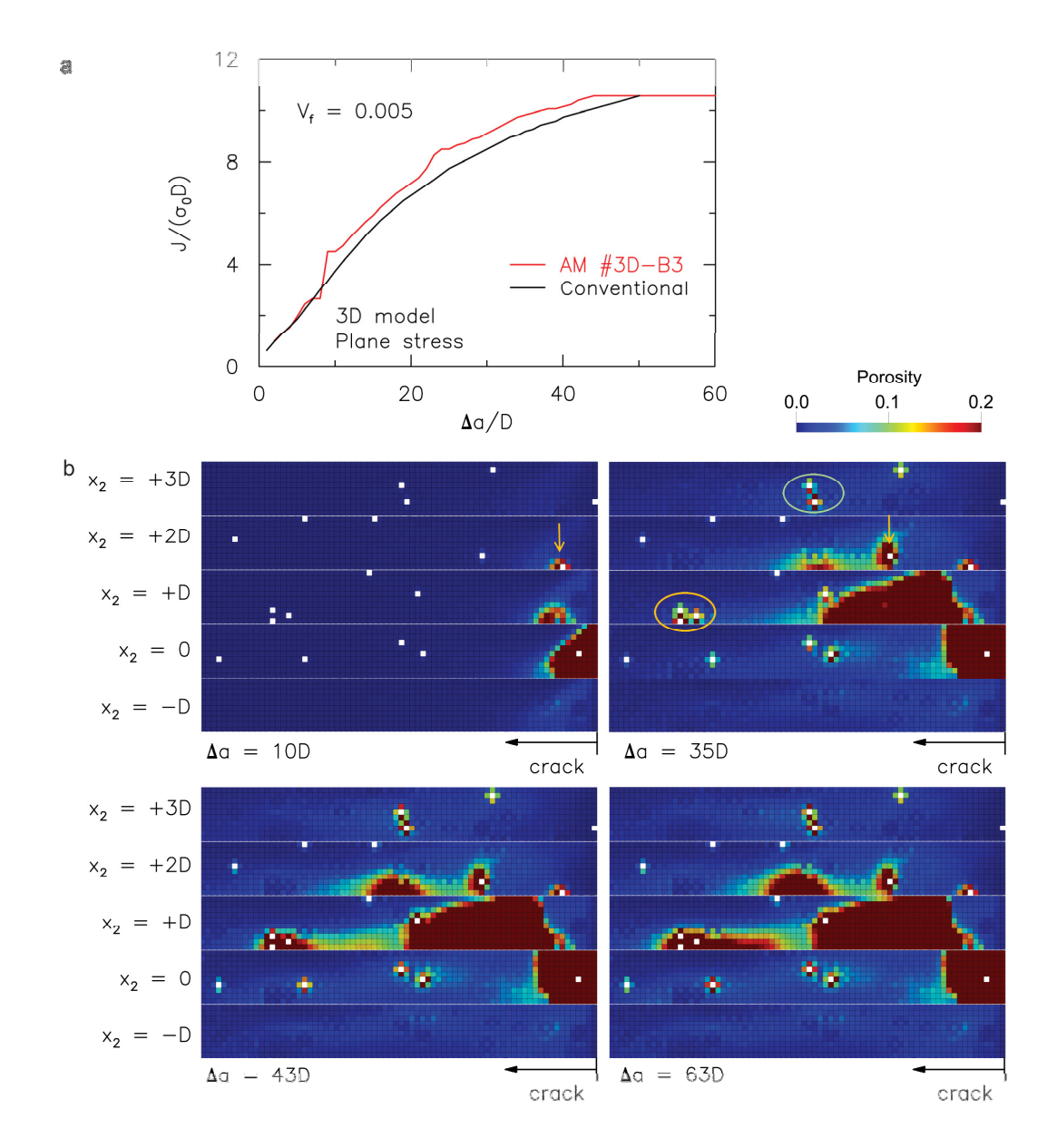


FIG. 10: Crack-defect interaction for plane stress AM model #3D-B3 with $V_f = 0.005$. (a) Fracture resistance curve. (b) Damage maps at $\Delta a = 10D$, 35D, 43D, and 63D. White squares denote the AM voids.

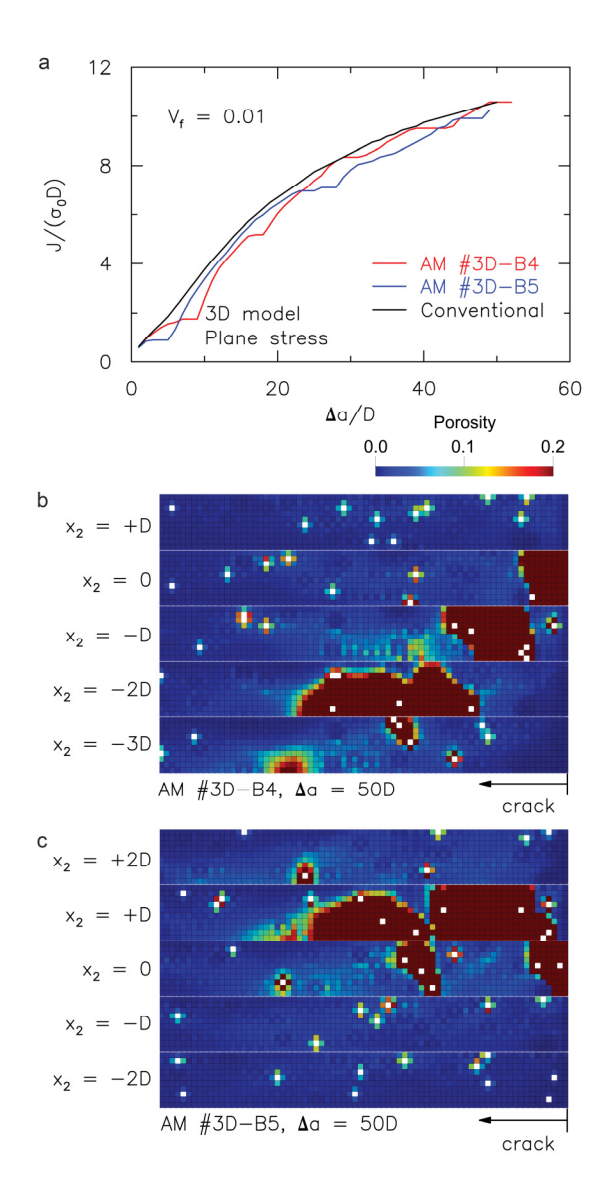


FIG. 11: Crack-defect interaction for plane stress AM models #3D-B4 and #3D-B5 with $V_f = 0.01$. (a) Fracture resistance curves. (b,c) Damage maps at $\Delta a = 50D$. White squares denote the AM voids.

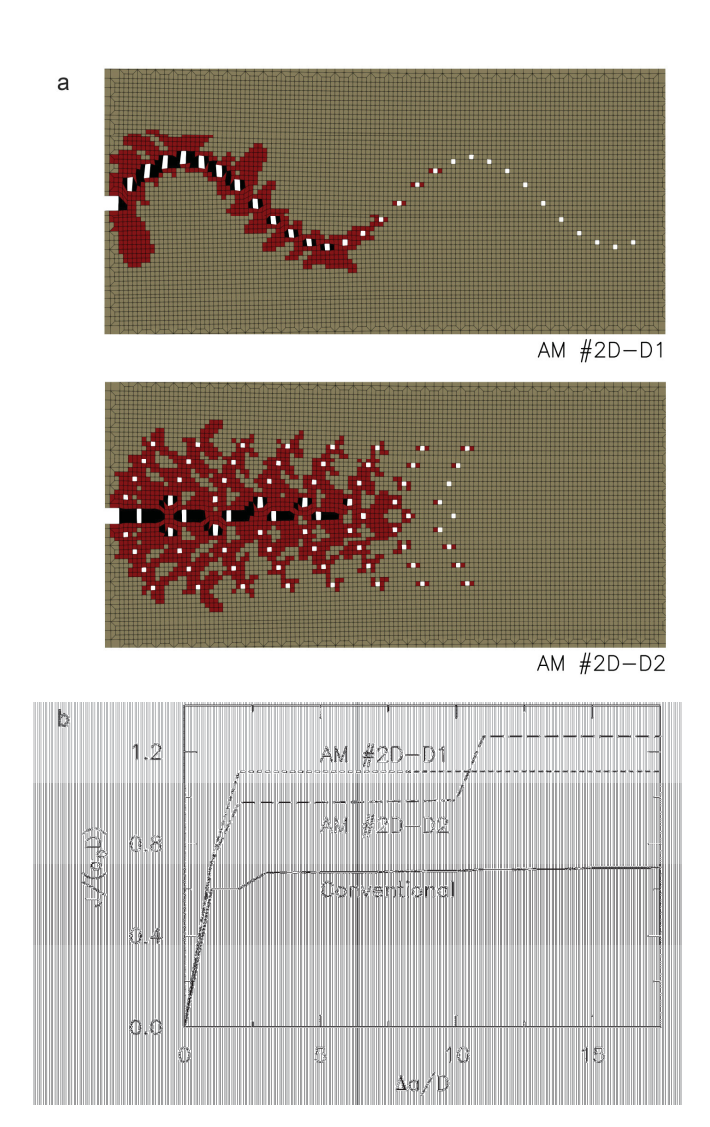


FIG. 12: AM void placement strategies for two plane strain 2D AM models (#2D-D1, #2D-D2). (a) Accumulated plastic strain contours. White squares denote the AM voids. (b) Fracture resistance curves.